EXPERIMENTAL CHARACTERIZATION OF A DIRECT METAL DEPOSITED COBALT-BASED ALLOY ON TOOL STEEL FOR COMPONENT REPAIR

Xinchang Zhang*, Tan Pan*, Wei Li*, Frank Liou*

*Department of Mechanical & Aerospace Engineering, Missouri University of Science and Technology, Rolla, Missouri, 65409, USA

Abstract

Die casting dies made of tool steel is subject to impact, abrasion and cyclic thermo-mechanical loading that delivers damage such as wear, corrosion, and cracking. To repair such defects, materials enveloping the damage need to be machined and refilled. In this study, V-shape defects with varied sidewall inclination angles were prepared on H13 tool steel substrates and refilled with cobalt-based alloy using direct metal deposition (DMD) for superior hardness and wear resistance. The microstructure of rebuild samples was characterized using an optical microscope (OM) and scanning electron microscope (SEM). Elemental distribution from the substrate to deposits was analyzed using energy dispersive spectrometry (EDS). Mechanical properties of repaired samples were evaluated by tensile test and microhardness measurement. Fracture mechanism in tensile testing was analyzed by observing the fracture surface. The experiment reveals that V-shape defects with sidewall beyond certain angles can be successfully remanufactured. The deposits were fully dense and free of defects. The microstructure and tensile test confirm the solid bonding along the interface. The tensile test shows the mean ultimate tensile strength (UTS) of repaired samples is approximated 620 MPa, where samples fractured at the deposits region. Hardness measurement reveals the hardness of deposits is around 810 HV which is much higher than that of the substrate.

Keywords: Direct metal deposition; Repair; Co-based alloy; Tool steel

Introduction

Laser-aided Direct Metal Deposition (DMD) is a relatively new technique but has shown great applications in the fields of part fabrication [1], [2], surface coating for improved wear and corrosion resistance [3], [4], joining different materials [5]–[7], deposit high-entropy alloys [8] and functionally gradient material [9]–[11] and part remanufacturing [12]–[17]. Depositing or cladding hard surfacing alloys on components through DMD process can modify the surface properties to greatly enhance hardness, wear and corrosion resistance, therefore, extending the service life of metallic components. When defects were observed on worn components, materials with better failure resistance can be welded in the damaged area to assure that the remanufactured parts will last a long time.

Cladding hard surfacing alloys such as Ni-based, Co-based alloys and WC composite has been widely investigated. Paul et. al. reported in [18] that they are able to produce fully dense and crack-free W-C-Co coatings on low carbon steel using pulsed Nd: YAG laser with an excellent bi-material bonding and much higher hardness. Zhong et. al. investigated the microstructure evolution during laser cladding of mixture of Stellite 6 and WC powder. In the coating of W-C-Co alloys on

medium carbon steel [19], the researchers observed some defects like pores and cracks in the clad layers mainly owing to gas entrapped in clad layers and stress concentration. Spherotene tungsten carbides were deposited on low carbon steel in [20]. The analysis exhibits a uniform distribution of hard particles in coatings with a hardness around 1000-1500 HV. Investigators in [20] coated 1.0 – 3.3 mm thick Co-based coatings on cast iron by optimizing processing parameters. The result reveals crack-free and good mechanical performance deposits.

Defects such as cracks, dents, pitting are commonly observed in worn components. In order to repair such defects, it is usually required to machine a slot or groove to remove materials around such damage to reveal a regular shape. In machining the slot, the sidewall inclination angle of the slot should be carefully determined. This is because the sidewall tilt angle may affect the bonding condition of filler material and substrate. A small tilt angle assures the accessibility of the target area but may result in much material removal. Because the removed material needs to be rebuilt through deposition, a large amount of material removal is not suggested. However, if the sidewall tilt angle is large, the bonding between deposits and substrate at the vertical surface cannot be guaranteed. Therefore, the slot sidewall inclination angle should be studied so that less material will be removed to get rid of defects and assure the bi-material bonding is solid.

This paper has two objectives. The first is to investigate the feasibility of direct metal deposition of a Co-based alloy Wallex 50 on tool steel for repair purpose. Besides, this papers aims to study the influence of sidewall inclination angle of defects on the properties of repaired coupons. In order to perform repair process, V-shaped defects with sidewall inclination angle of 45°, 75° and 90° were prepared on H13 tool steel substrates. The missing volume of each substrate is reconstructed by scanning the damaged part using a structured-light 3D scanner. After that, the missing geometry was sliced into layers to generate a raster deposition tool path. Wallex 50 material was added to the damaged region to regain the missing geometry. In order to test the repair quality, macrostructure and microstructure characterization, EDS and XRD analysis, tensile test and microhardness measurement were performed on the repaired samples.

Experimental condition and procedure

Material and preparation

H13 tool steel is usually used for manufacturing die casting dies owing to its great thermal fatigue cracking resistance. Therefore, H13 tool steel plate with dimensions of 25 mm × 10 mm × 15 mm was selected as the substrate material. In order to perform repair experiments, several V-shaped grooves with different sidewall inclination angles were machined on the substrates. Three sidewall inclination angles of 45°, 75°, 90°, were chosen which are depicted in Fig. 1a-c. The depth of each groove is 7 mm and the width of defects at the bottom is 5 mm. The chemical compositions of H13 tool steel are listed in Table 1.

Wallex 50 is chosen as the filler material because it is a Co-based hard surfacing alloy with excellent corrosion resistance and low coefficient-of-friction, providing good metal-to-metal wear protection. Wallex 50 has high contents of Co, Ni, Cr, and W to guarantee a high hardness as well as good corrosive resistance. Wallex 50 can be coated on easy-to-wear surfaces of H13 tool steel dies to enhance its resistance to wear. Therefore, this paper tries to evaluate the repair quality of

using Wallex 50 as a deposition material. The chemical compositions of Wallex 50 are collected in Table 1. Wallex 50 alloys powder was characterized to analyze particle shape and size distribution. An SEM micrograph of Wallex 50 alloys powder was obtained and presented in Fig. 2a. The image reveals that most powder particles are spherical although a few of them have irregular shapes. Particle size distribution analyzed using ImageJ shows the average particle diameter is 65 µm (Fig. 2b).
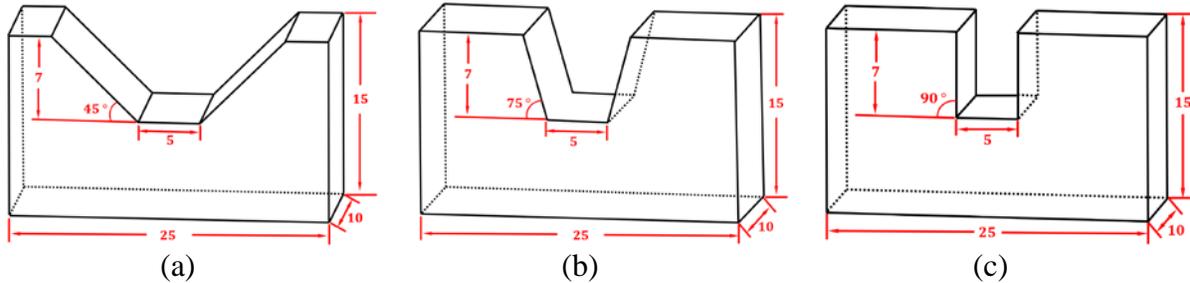

<center>(a)   (b)   (c)</center>

Fig. 1 Dimensions of the prepared substrates with (a) 45°, (b) 75° and (c) 90° sidewall inclination angle

Table 1 Chemical composition of the target materials (wt%)

Materials	C	Mn	Si	Cr	Ni	Mo	V	W	B	Fe	Co
H13 tool steel	0.4	0.4	1.0	5.25	-	1.35	1.0	-	-	Bal.	-
Wallex 50	0.8	-	2.75	19	18	-	-	10	3.4	1.0	Bal.

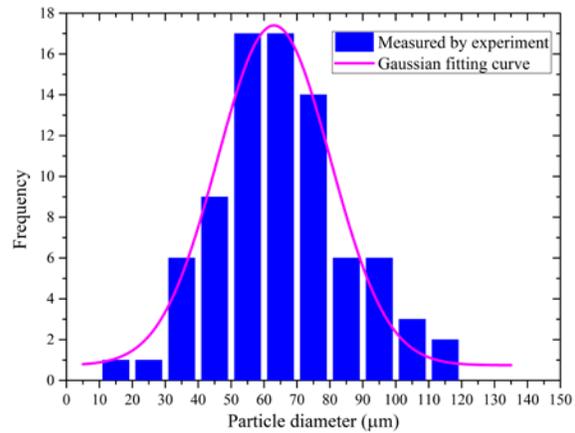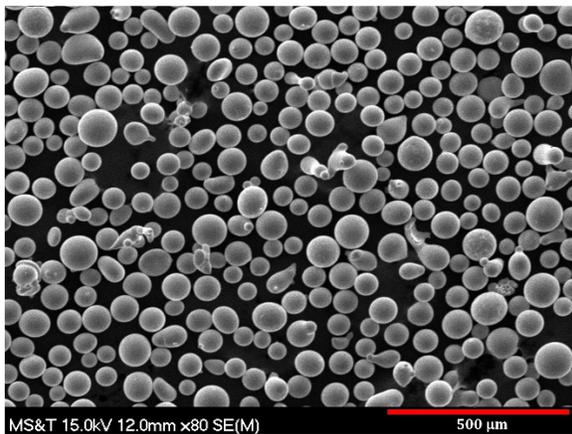<center>(a)   (b)</center>

Fig. 2 SEM micrograph (a) and particle size distribution (b) of Wallex 50 powder

Experimental setup

When V-shaped defects were prepared on the substrate, it is necessary to obtain the geometry of the missing volume to generate additive tool path. This deposition tool path directly determines the shape of restored parts and has great effects on the mechanical properties of deposits. To make sure the acquired dimensions of the refill volume is accurate, an RE-based damage extraction process was conducted. Each substrate was scanned using a high accuracy

structured-light metrology 3D scanner (OptimScan 5M from Shining 3D Tech. Co. Ltd., Fig. 3a) to reconstruct its three-dimensional model. The principle of the structured-light scanner is shown in Fig. 3a where a pattern with stripes was projected on an object by the structured-light projector and two CCD cameras on the left and right of the scanner capture the distortions of the pattern. The distortion of pattern reveals the three-dimensional geometry of the object. A complete scan of the part requires scanning of the geometry in different orientations and therefore, indexing targets were randomly marked on the part so that multiple scans can be registered into a single model.

Substrates with different sidewall inclination angles were scanned using the configuration and the scanned point cloud was presented in Fig. 3b. Defining the point set in the damaged region is simply conducted by calculating the distance between each point to the top surface. The points on peripheral surfaces around the substrate are not considered as damage. After damaged point searching, the missing geometry can be defined, which is depicted in Fig. 3c. One can see in Fig. 3c that the damage for the sample with 90° sidewall defects was not completely scanned because the vertical sidewall combined with narrow slot blocks the two cameras from capturing projected pattern simultaneously. However, this uncomplete scanned point data has no effect on the additive tool path generation because the tool path generation algorithm relies on the convex-hull of the data set, which is described below.

After the damage was extracted, tool path was generated based on damaged point cloud utilizing the algorithm introduced in [21]. The damaged point set was sliced into 11 layers with a layer thickness of 0.6 mm. For each layer, deposition tool path was planned which comprises outline contour and raster infill pattern, indicating laser moves along the enveloping boundary and then along the zigzag pattern to acquire fully dense deposits. The tool path for three scenarios was shown in Fig. 4a-c.

After additive tool path was acquired, the damaged substrates were loaded to DMD system for material deposition. The DMD cell employed in this study (Fig. 5) includes a 1000 W peak power continuous wave fiber laser, gas-assisted blown powder feeder (Model 1200, Bay State Surface Technologies, Inc.), 3-axis work table and Argon gas feeding unit. The laser has a beam diameter of 1.8 mm. The laser beam is tilted while the powder feed nozzle is vertical with a stand-off distance of 10 mm. The welding was performed in argon gas environment to keep weld beads from oxidization. The processing parameters were summarized in Table 2.
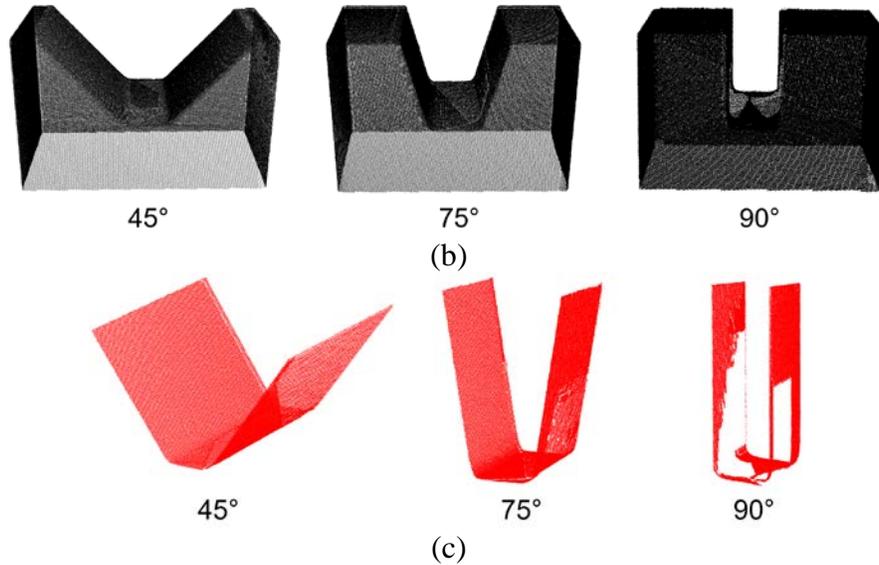

(a)
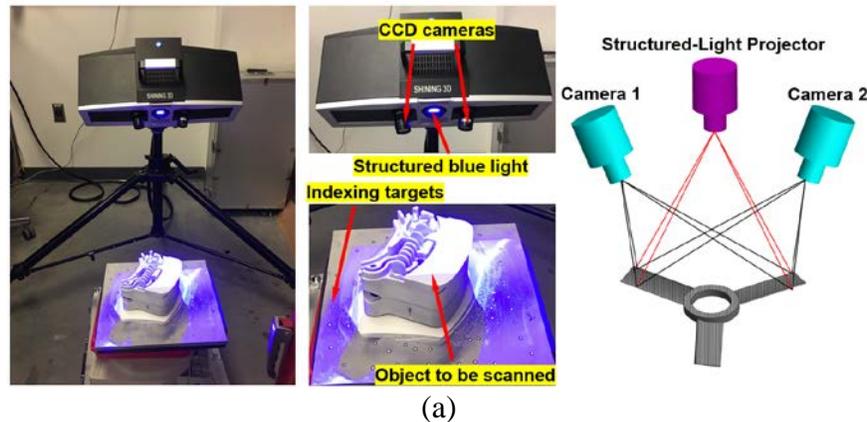
Fig. 3 Model reconstruction for repair volume determination; (a) 3D scanning setup; (b) Reconstructed point cloud data; (c) Extracted damaged point set
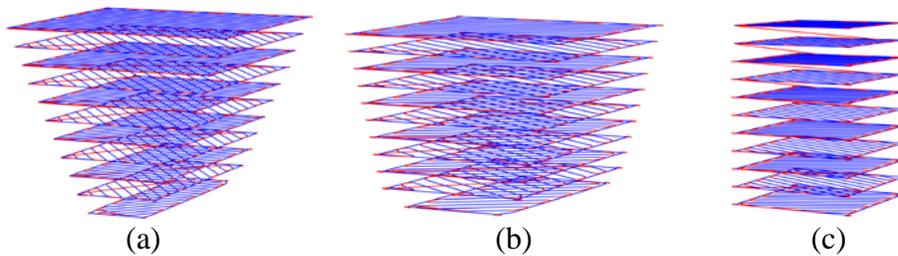

Fig. 4 Repair tool path for substrates including defects with (a) 45°, (b) 75° and (c) 90° sidewall inclination angle
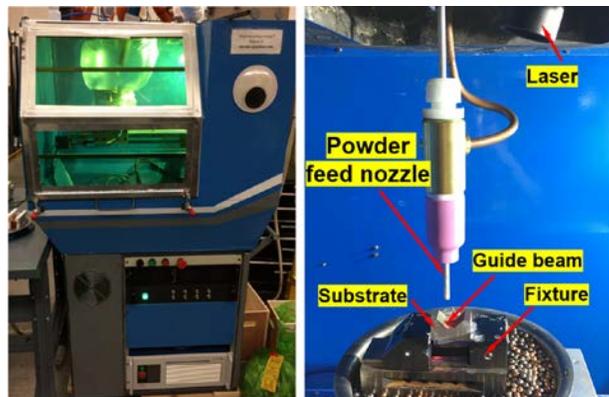

Fig. 5 DMD system and setup

Table 2 Component repair processing parameters

Laser power (W)	Powder flow rate (g/min)	Layer thickness (mm)	Scan speed (mm/min)	Overlap
350	3.2	0.6	220	0.5

Sample preparation and material characterization

Repaired samples were sliced into layers using Hansvedt electric discharge machine (EDM) and mounted on Bakelite using Simplimet 1000 mounting equipment. Specimens were ground using abrasive papers from 120 Silicon Carbide Grid to 1200 Grid and finally polished using 0.05 microns silica suspension and then ultrasonically cleaned. The prepared samples were macroscopic analyzed using HIROX KH-8700 optical microscope to study the fusion boundary between refilled material and substrates. After that, the microstructure of deposits near the interface was revealed using Hitachi S4700 Scanning Electron Microscope (SEM). EDS line scan analysis was performed from the deposits to substrates to reveal elemental distribution.

In order to test the mechanical properties of the repair coupons, tensile test and hardness measurement were conducted. For tensile test, the samples were cut into thin layers with a thickness of 1 mm as shown in Fig. 6. Tensile specimens were cut from each thin slices using EDM. The dimensions of tensile specimens are shown in Fig. 6c. The position and orientation of tensile samples were depicted in Fig. 6a-b. Each tensile specimen consists of deposits and substrate, with interface locating at the middle of the specimen. The tensile test was conducted using Instron tester (Model 3300) with a crosshead speed of 0.015 mm/min (Fig. 6d). Ultimate tensile strength was obtained and then, tensile fracture surface was analyzed. Vickers hardness was measured using Struers Duramin hardness tester with a press load of 9.81 N and dwell time of 10s.
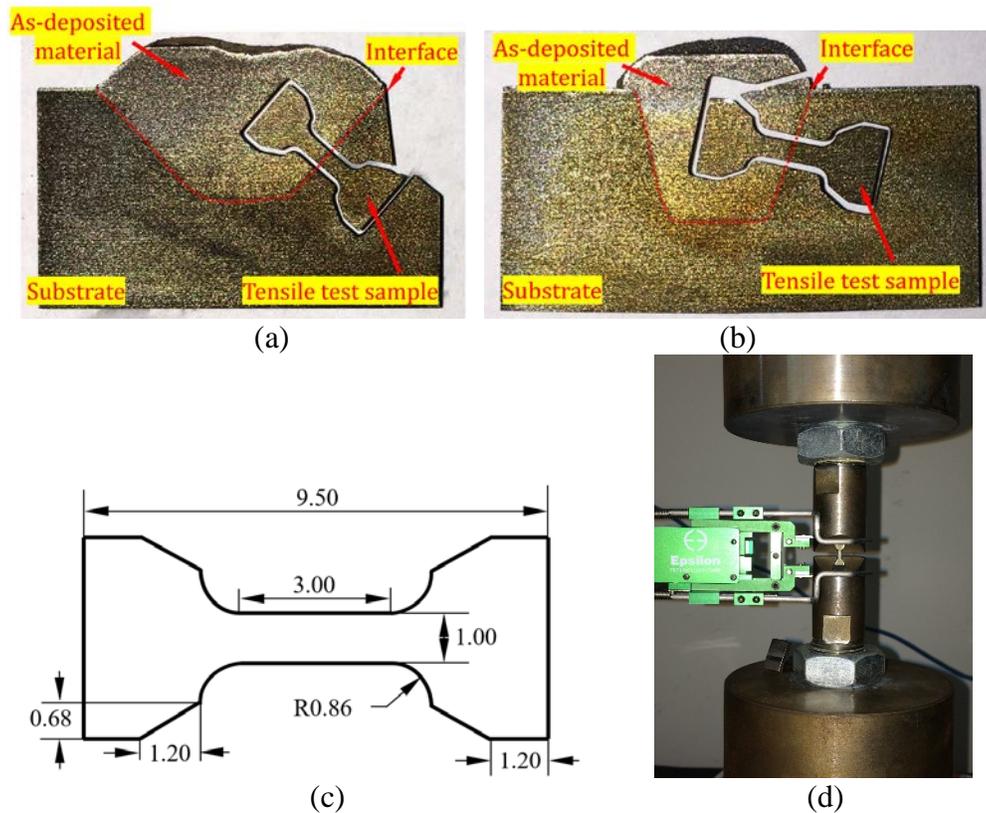

Fig. 6 Tensile test specimen preparation and setup; Tensile specimen over the sectioned repaired substrates with 45° (a) and 75° (b) sidewall inclination angle damage; (c) Dimensions of the tensile test specimen (Dimensions in mm, 1mm in thickness); (d) Tensile test setup

Results and discussion

Visual and Macrostructure

The overview of the repaired samples is shown in Fig. 7. It seems that missing volumes on all substrates were refilled successfully. However, by deeper visual observation, one can see the refilled region on the sample with 90° sidewall defects was not fully dense. A big hole was observed slightly at the right portion of deposits. This is because when the laser was melting the materials on the side vertical surface, filler material was not able to bond with the substrate and fell down, which caused the hollow space inside the deposits. This is validated by observing the cross-sections of samples discussed below.

The optical micrographs of cross-sections of the repaired samples are depicted in Fig. 8a-c, which has sidewall inclination angle of 45°, 75°, and 90°, respectively. Micrographs were taken at the boundary of deposits and substrate. One can realize that the bonding line is free of defects for 45° and 75° samples, while a large number of porosities and lack of fusion were observed in the sample with 90° tilt sidewall damage. Those defects were almost entirely located along the sidewall boundaries. The bottom region of the 90° tilt sidewall sample, however, is well bonded. This phenomenon is expected because, for a vertical sidewall, the laser cannot continuously melt the materials at the vertical side of the defects but can still effectively melt materials on the bottom region. Thus, melt poor cannot be successfully formed at vertical regions and filler materials were not able to be melt and deposited. This situation might be addressed by using 5-axis DMD system by rotating the substrate so that the sidewall is relatively accessible to the laser beam. However, this is not always working if the defects are deep and narrow. Besides, toolpath planning for 5-axis DMD system is much complicated and only desired if really required.
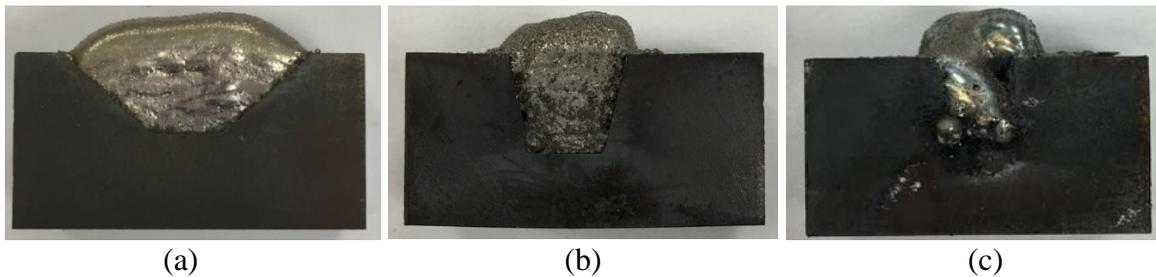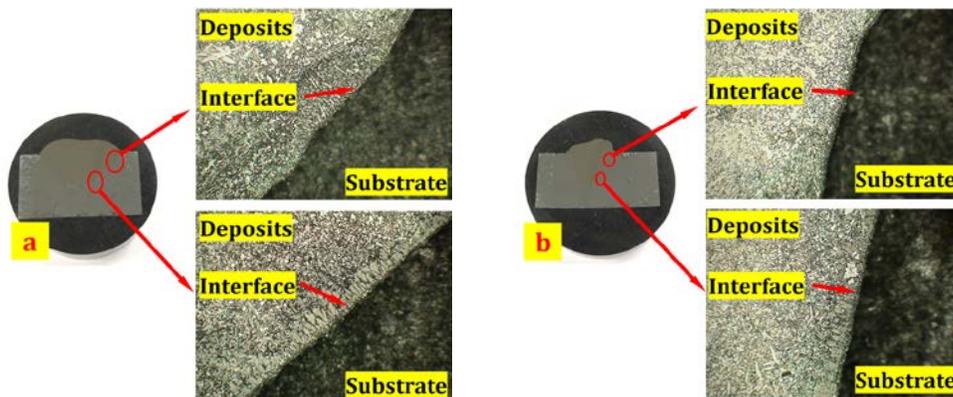

| (a) | (b) | (c) |

Fig. 7 Overview of the repair samples with 45° (a), 75° (b) and 90° (c) sidewall inclination angle
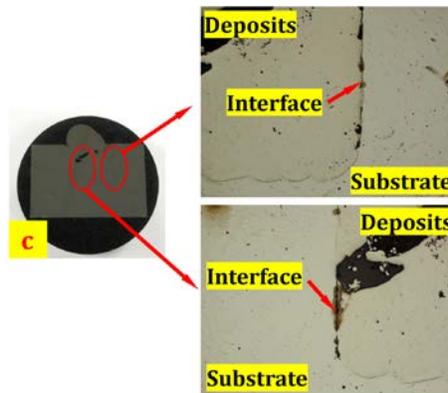
Fig. 8 Optical micrographs of cross-sections of the repaired samples with 45° (a), 75° (b) and 90° (c) sidewall inclination angle damage

Microstructure characterization and EDS analysis

Because the defective substrate with 90° sidewall inclination angle was failing to repair, only samples with 45° and 75° sidewall damage were further analyzed in terms of microstructure and mechanical properties. Microstructure images were taken at the boundary of deposits and substrates, as shown in Fig. 9. The images distinctly show the bi-material boundary line. The microstructure changed sharply from the substrate to deposits. This is no smooth transitional region between two materials. By observation, one can see there are no defects such as cracks, pores, or delamination observed along the interface, confirming the solid bonding condition. The SEM images reveal that deposits were metallurgically bonded with the substrate. The tensile test in the following of this paper also validated the sound bonding.

The SEM micrographs in Fig. 9 also shows that the microstructure of deposits near the interface mostly consists of columnar structure stretched towards to the center of deposits. Those grains were growing parallel to the heat flow direction during solidification. When starting to deposit the first few layers, the damaged substrate was at room temperature. The laser melted a tiny amount of material on the substrate, forming a melt pool, and when materials were injected into such region and laser moved away, the cooling rate at such area is extremely high, which caused the grain to grow in the columnar direction. The cooling is so fast that leaves not sufficient time for grains to form secondary dendrites. As materials were deposited layer by layer, the microstructure of deposits gradually changed to dendrite with interdendritic eutectics. This results from the dropped cooling rate when depositing the above layers.

The microstructure of top layers of as-deposited Wallex 50 alloy is presented in Fig. 9c, which consists of mostly interdendritic eutectics. It was observed that the gray region was enveloped by bright phases. EDS spectrum shows the bright region in Fig. 9c was rich in Cr and W and the gray area is dominated by Co, Ni, and Si.

EDS line scan was performed on the repaired samples to study elemental composition and distribution. The obtained data are plotted in Fig. 10. The scan was started from the deposits and ended in the region of the substrate, passing through the bi-material interface. Major elements of Co and Fe were quantified along this path. Dwell time for each scanned point was 200 ms.

EDS line scan exhibits the major elements like Co and Fe were gradually changed when passing the interface. This is because, when a melt poor was created on the substrate, Co-based alloy Wallex 50 was filled in the melt poor and mixed with the melted H13 tool steel material. Such mixed regions caused the elemental distribution changing near the interface. Relatively large amount of Fe exists in the first few layers of deposits, showing the dilution of Fe into Wallex 50. Therefore, Fe contributes to the phase transformation over the interface. The EDS line scan result confirms that excellent metallurgical fusion was created through the interface.
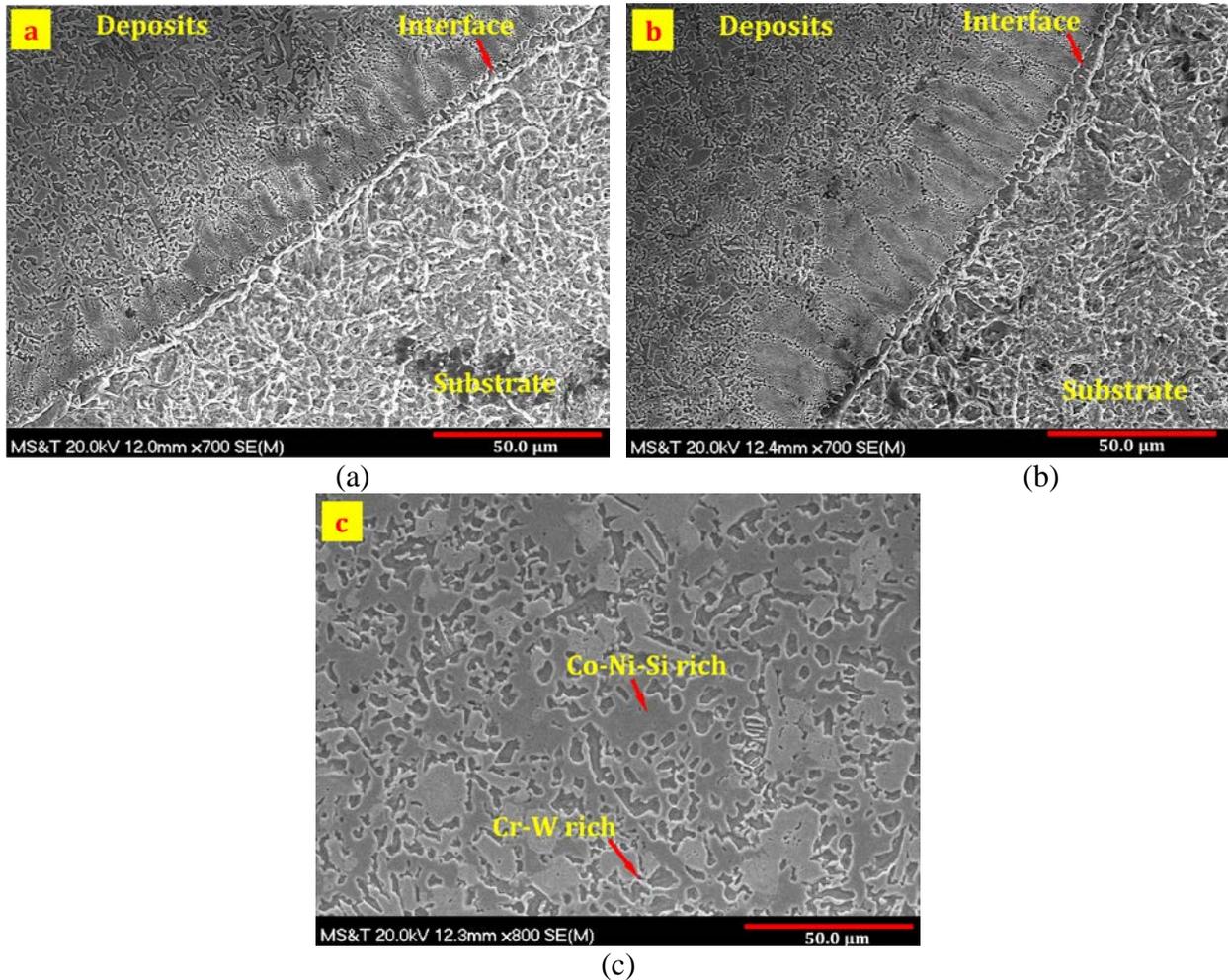

(a)   (b)

(c)

Fig. 9 SEM micrographs of the boundary area of repaired samples with 45° (a) and 75° (b) sidewall damage; (c) Micrographs of top layers of the repaired sample with 45° sidewall damage
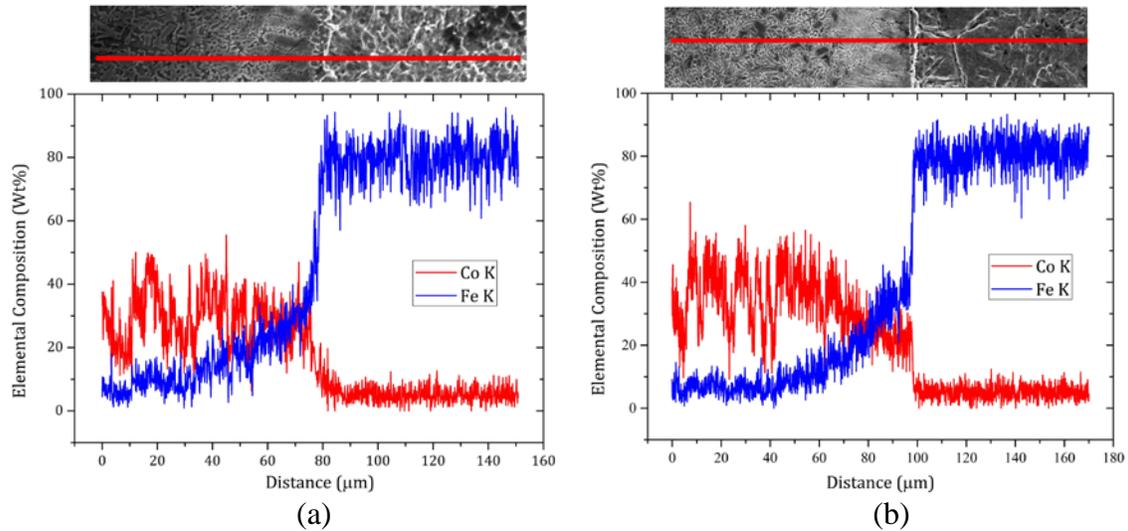
Fig. 10 EDS line scan analysis results for samples with 45° (a) and 75° (b) damage

Mechanical properties

Tensile behavior and tensile fracture surface

The tensile stress-strain curves for two repaired samples were plotted in Fig. 11 and the Ultimate Tensile Strength (UTS) is summarized in Table 3. The tensile stress-strain curves reveal that the tensile stress increased with the increase of tensile strain to a maximum stress of about 620 MPa, and then, the tensile samples fractured suddenly and the stress decreased rapidly. The curves didn't reveal yielding phenomenon during the tensile testing. The ductility of tensile samples was extremely low. Further investigation reveals all samples fractured at the as-deposited Wallex 50 region. Therefore, the as-deposited Wallex 50 alloy shows brittle failure mechanism.

The average UTS of the repaired samples with 45° and 75° V-shaped defects is approximately 618 MPa and 624 MPa, respectively. The tensile testing shows the influence of sidewall inclination angle on the UTS is barely recognizable. There is a relatively big variation of UTS in the tested result. This variation was possibly attributed to the unevenly located defects in the deposited regions. Some micropores in deposits may affect the UTS and result in such standard deviation.

The micrographs of tensile fracture surface are presented in Fig. 12a-c. The overview image reveals a relatively flat surface which is perpendicular to the tensile loading direction. Magnified view in Fig. 12b-d shows microscopically unsmooth areas. Microcracks were observed at such magnified views. There is a very limited population of voids and dimples, indicating the fractured region is very brittle. This is because the Wallex 50 is a Co-based alloy and also consist of a relatively large number of hard elements including Cr, W, Si. Cr, W, and Si can form a very hard phase that results in the brittle failure mechanism of as-deposited Wallex 50 during tensile testing.
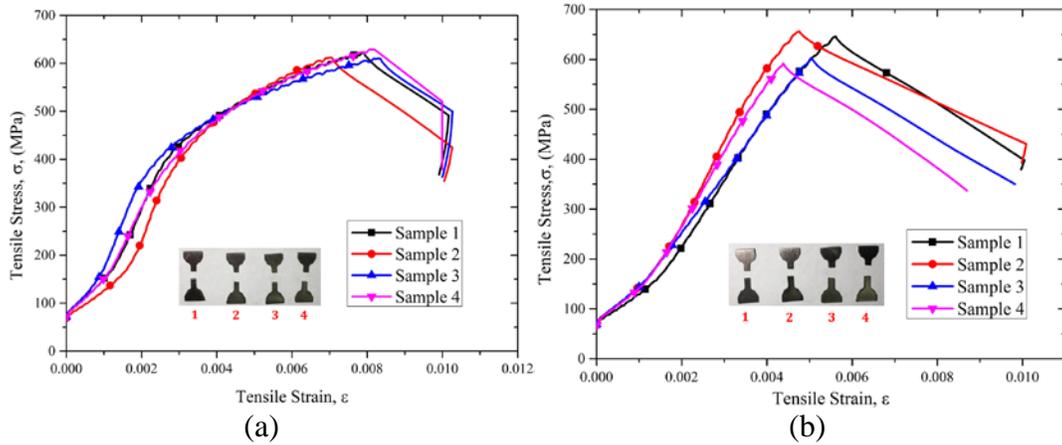
(a)   (b)

Fig. 11 Tensile stress-strain curves for repaired samples with 45° U-shaped defects (a) and 75° U-shaped defects (b)

Table 3 UTS obtained from tensile test

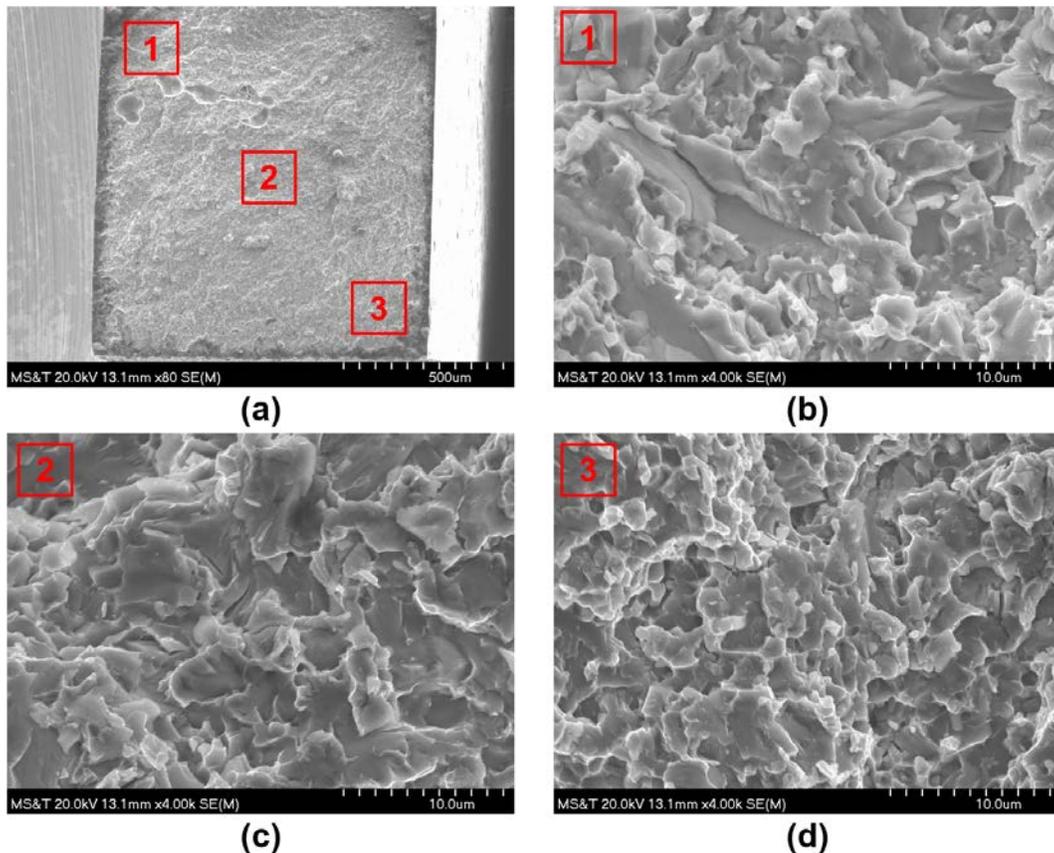|	Specimen	UTS (MPa)
	1	623.06
	2	612.12
	3	610.00
45°	4	629.46
	Average	618.66
	S.D.	9.19
	1	646.22
	2	656.36
	3	602.61
75°	4	591.73
	Average	624.23
	S.D.	31.83

Fig. 12 Tensile fracture morphologies; (a) Overview of the fracture surface; (b) Magnified view of area 1 in (a); (c) Magnified view of area 2 in (a); (d) Magnified view of area 3 in (a)

Microhardness measurements

Vickers hardness was measured on the cross-sections of the repaired samples starting from the top of deposits to the substrate. The step between two adjacent indentations is 0.4 mm. The Vickers hardness tested on two samples was plotted in Fig. 13.

A first observation is that the hardness of deposits is much higher than the hardness of substrate. The hardness of the H13 substrate is approximately 210 HV, while the hardness of deposits is 810 HV, almost four times of the hardness of substrate. However, H13 tool steel used for die casting dies is in quenched and tempered condition and usually shows a hardness range of 480 -520 HV. The reason that the hardness of the substrate utilized in this study is only 210 is owing to the condition of the received H13 tool steel material. The as-received H13 substrate is in the annealed condition and has not been hardened, causing the low hardness. However, one can see that even the hardened H13 tool steel which condition is exactly used for casting dies is also much lower than the hardness of as-deposited Wallex 50.

The sharply increased hardness on the deposited region is mainly caused by two reasons. The major reason is that Wallex 50 is a Cobalt-based Co-Ni-Cr-W alloy. The Cobalt-rich matrix with very hard phases results in the very high hardness. In addition, the cooling rate during material deposition is rapid, leading to the formation of fine microstructure, which also plays a role in the

hardening. The hardness at bi-material interface jumped from 250 HV to 800 HV rapidly. The transitional hardness values at interface indicate the dilution in the heat-affected area. The transitional range is approximately 1.5 mm.
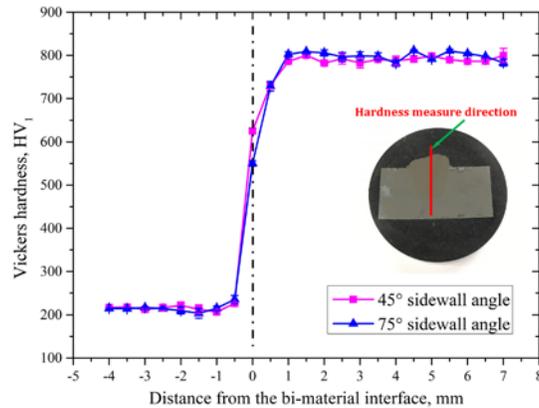

Fig. 13 Vickers hardness tested on the cross-section of the repaired samples

Conclusion

In the current study, Co-based alloy Wallex 50 was evaluated through depositing on H13 tool steel substrate. In order to test the possibilities of repairing slots with different sidewall inclination angles, V-shaped defects with 45°, 75°, and 90° sidewall tilt angles were prepared. The tool path for material deposition was obtained through 3D scanning of the defective substrate and extracting the damaged area. Once the missing volume was obtained, it was sliced into layers to generate a raster deposition tool path. Wallex 50 particles were filled up the missing area to regain the geometry. To validate the repair quality, a number of tests were performed on the repaired samples.

The macroscopic analysis confirms the samples with 45° and 75° damage were repaired successfully. For the sample with 90° damage, since the laser was not able to melt the material at the vertical area, filler material was not bonding well with the substrate, causing lack of fusion and a large number of pores. The microstructure of deposits near interface shows mostly columnar structure mainly due to the high cooling rate for the first few layers. As materials built up layer by layer, microstructure was changed to the equiaxed structure. Microstructure and EDS analysis confirm the forming of metallurgical bonding along the interface.

Tensile testing of repaired samples reveals a UTS of approximately 620 MPa. The influence of sidewall inclination angle of damage on the UTS is not observed. The fracture surface shows all samples fractured at the as-deposit Wallex 50 region and shows brittle failure mechanism. The hardness analysis shows deposits is much harder than the substrate. A homogeneous hardness of 810 HV was measured on deposits while the hardness of substrate is around 210 HV.

Acknowledgment

Reference

[1]   E. C. Santos, M. Shiomi, K. Osakada, and T. Laoui, "Rapid manufacturing of metal components by laser forming," *Int. J. Mach. Tools Manuf.*, vol. 46, no. 12–13, pp. 1459–1468, Oct. 2006.

[2]   N. Hopkinson and P. Dickens, "Rapid prototyping for direct manufacture," *Rapid Prototyp. J.*, vol. 7, no. 4, pp. 197–202, 2001.

[3]   L. Thivillon, P. Bertrand, B. Laget, and I. Smurov, "Potential of direct metal deposition technology for manufacturing thick functionally graded coatings and parts for reactors components," *J. Nucl. Mater.*, vol. 385, no. 2, pp. 236–241, 2009.

[4]   F. Weng *et al.*, "Effect of process parameters on the microstructure evolution and wear property of the laser cladding coatings on Ti-6Al-4V alloy," *J. Alloys Compd.*, vol. 692, pp. 989–996, 2017.

[5]   W. Li, L. Yan, X. Chen, J. Zhang, X. Zhang, and F. Liou, "Directed energy depositing a new Fe-Cr-Ni alloy with gradually changing composition with elemental powder mixes and particle size' effect in fabrication process," *J. Mater. Process. Technol.*, vol. 255, pp. 96–104, 2018.

[6]   W. Li, X. Chen, L. Yan, J. Zhang, X. Zhang, and F. Liou, "Additive manufacturing of a new Fe-Cr-Ni alloy with gradually changing compositions with elemental powder mixes and thermodynamic calculation," *Int. J. Adv. Manuf. Technol.*, Nov. 2017.

[7]   Z. Lei, Z. Tian, P. Li, Y. Chen, H. Zhang, and X. Chen, "Joining of Sip/6063Al composite using additive manufacturing-based laser melting deposition," *Mater. Lett.*, vol. 190, pp. 191–194, 2017.

[8]   W. Cui, X. Zhang, and F. Liou, "Additive Manufacturing of High-Entropy Alloys Œ A Review," *Solid Free. Fabr. Symp.*, pp. 712–724, 2017.

[9]   W. Li, J. Zhang, X. Zhang, and F. Liou, "Effect of optimizing particle size on directed energy deposition of Functionally Graded Material with blown Pre-Mixed Multi-Powder," *Manuf. Lett.*, vol. 13, pp. 39–43, 2017.

[10]   W. Li, X. Zhang, and F. Liou, "Modeling analysis of argon gas flow rate's effect on pre-mixed powder separation in laser metal deposition process and experimental validation," *Int. J. Adv. Manuf. Technol.*, vol. 96, no. 9, pp. 4321–4331, Jun. 2018.

[11]   W. Li, J. Zhang, X. Zhang, and F. Liou, "Effect of Optimizing Particle Size on Directed Energy Deposition of Functionally Graded Material with Blown Pre-mixed Multi-powder," 2017.

[12]   X. Zhang, W. Li, K. M. Adkison, and F. Liou, "Damage reconstruction from tri-dexel data for laser-aided repairing of metallic components," *Int. J. Adv. Manuf. Technol.*, vol. 96, no. 9, pp. 3377–3390, Jun. 2018.

[13]   X. Zhang, W. Cui, W. Li, and F. Liou, "Metallic Components Repair Strategies Using the Hybrid Manufacturing Process," *Solid Free. Fabr. Symp.*, pp. 1862–1876, 2017.

[14]   F. Liou, K. Slattery, M. Kinsella, J. Newkirk, H. Chou, and R. Landers, "Applications of a hybrid manufacturing process for fabrication of metallic structures," *Rapid Prototyp. J.*, vol. 13, no. 4, pp. 236–244, 2007.

[15]   X. Zhang, W. Li, W. Cui, and F. Liou, "Modeling of worn surface geometry for engine

blade repair using Laser-aided Direct Metal Deposition process," *Manuf. Lett.*, vol. 15, pp. 1–4, 2018.

[16]   X. Zhang, W. Li, and F. Liou, "Damage detection and reconstruction algorithm in repairing compressor blade by direct metal deposition," *Int. J. Adv. Manuf. Technol.*, vol. 95, no. 5, pp. 2393–2404, Mar. 2018.

[17]   X. Zhang, W. Li, X. Chen, W. Cui, and F. Liou, "Evaluation of component repair using direct metal deposition from scanned data," *Int. J. Adv. Manuf. Technol.*, pp. 1–14, 2017.

[18]   C. P. Paul, H. Alemohammad, E. Toyserkani, A. Khajepour, and S. Corbin, "Cladding of WC-12 Co on low carbon steel using a pulsed Nd:YAG laser," *Mater. Sci. Eng. A*, vol. 464, no. 1–2, pp. 170–176, 2007.

[19]   Y. Yang and H. C. Man, "Microstructure evolution of laser clad layers of W–C–Co alloy powders1This paper is sponsored by The Natural Science Foundation of Guangdong Province, China.1," *Surf. Coatings Technol.*, vol. 132, no. 2, pp. 130–136, 2000.

[20]   J. M. Amado, M. J. Tobar, J. C. Alvarez, J. Lamas, and A. Yáñez, "Laser cladding of tungsten carbides (Spherotene®) hardfacing alloys for the mining and mineral industry," *Appl. Surf. Sci.*, vol. 255, no. 10, pp. 5553–5556, 2009.

[21]   R. Liu, Z. Wang, Y. Zhang, T. Sparks, and F. Liou, "A Smooth Toolpath Generation Method for Laser Metal Deposition," *Proc. 27th Annu. Int. Solid Free. Fabr. Symp. Austin, Texax, USA*, pp. 1038–1046, 2016.